Journal of Power Sources 360 (2017) 353–359

Contents lists available at ScienceDirect

Journal of Power Sources

journal homepage: www.elsevier.com/locate/jpowsour

Novel quantum dot and nano-sheet TiO_2 (B) composite for enhanced photocatalytic H_2 – Production without Co-Catalyst

Jingjing Si, Yu Wang***, Xiaohong Xia, Shuai Peng, Ying Wang, Shuying Xiao, Lingbin Zhu, Yuwen Bao, Zhongbing Huang**, Yun Gao*

Faculty of Materials Science & Engineering, Faculty of Physics & Electronic Technology, Hubei University, Wuhan, 430062, PR China

HIGHLIGHTS

- We produced a green 3.1-nm-thick TiO_2(B) nanosheets on a large scale.
- The efficiency of TiO_2(B) nanosheets is 23 times higher than that of P25.
- The conduction band edge of TiO_2(B) is 0.6 eV higher than that of anatase.
- The TiO_2(B)-anatase nanocomposites show catalytic rate of 1312 μmol h^{-1} g^{-1}.

ARTICLE INFO

Article history:
Received 12 April 2017
Received in revised form
2 June 2017
Accepted 6 June 2017

Keywords:
TiO_2 (B) nano-sheets
TiO_2 nanocomposite
Hydrogen production
Photocatalyst

ABSTRACT

Recently, the production of hydrogen through water splitting using titania (TiO_2) as photocatalyst has received great attention in the new energy field. In this work, a single one-step hydrothermal method is used to synthesize ultra-thin TiO_2 (B) nano-sheets, anatase TiO_2, and their composite, using ethylene glycol (EG) and ethanol as the solvent. A new composite nanostructure with anatase TiO_2 quantum dots grown on TiO_2 (B) nano-sheets is obtained at certain ratios between EG and ethanol. Even without the help of co-catalyst, a high photocatalytic efficiency, about 45 times of that of rutile-anatase mixed Degussa P25, is observed in the TiO_2 (B)-anatase composite nanostructure. The outstanding performance can be attributed to its large specific surface area, abundant surface active sites, mixed phase promoted efficient charge separation. Moreover, the properly aligned band structure, with the conduction band level of ultra-thin TiO_2 (B) about 0.6 eV higher than that of the anatase, provides a large driving force for the reduction of water.

1. Introduction

Since the discovery of water photolysis on a TiO_2 electrode under ultraviolet (UV) light irradiation in the 1970s, the study of solar hydrogen production based on photocatalyst has been being a hot topic in the material and energy fields [1–3]. Although some new photocatalysts have been found following TiO_2, it is still regarded as the most promising semiconductor photocatalyst, due to its advantages of high photocatalytic activity, chemical stability, low cost, and environmental friendliness [4–6]. To gain a high photocatalytic efficiency, the photocatalyst should have suitable band structure, effective charge separation and migration route for photo-generated carriers, enough surface active sites and surface area [7].

Among the TiO_2-based photocatalysts, the composite TiO_2 nanostructures have been demonstrated to have a higher photocatalytic activity compared to the single phase ones, since the heterojunction interface built between various phases provides a charge separation route [8–12]. For instance, several experiments showed that the anatase-rutile junction outperforms the individual polymorphs [12–15]. Electron paramagnetic resonance for the mixed anatase-rutile samples indicated that electrons flow from rutile to anatase, while holes move in the opposite direction [16,17]. However, because the conduction band level of TiO_2 (both anatase and rutile) is not high enough to directly reduce water to produce H_2 [4,15,18], co-catalysts, such as Pt, were usually loaded to provide

* Corresponding author.
** Corresponding author.
*** Corresponding author.
E-mail addresses: wyu@hubu.edu.cn (Y. Wang), huangzb@hubu.edu.cn (Z. Huang), gaoyun@hubu.edu.cn (Y. Gao).

http://dx.doi.org/10.1016/j.jpowsour.2017.06.021
0378-7753/

effective proton reduction sites for water, and also to suppress the charge carrier recombination [7,8,19]. The introduction of noble metal increases the cost of TiO_2-based photocatalyst and limits its applications at industrialized scale.

To gain a high efficient H_2 production for TiO_2 without the help of the co-catalyst, synthesis of TiO_2 nano-sheet is an effective way to ameliorate the above problems for its huge specific surface area, abundant surface Ti^{3+} as active sites and unique enlarged bandgap caused by quantum confinement effect [20–22]. Recently, a less symmetrical metastable TiO_2 (B) phase was found to have a monoclinic structure consisted of both edges and corners shared TiO_6 octahedra [23,24]. The layered crystal structure of TiO_2 (B) tends to form two-dimensional (2D) corrugated nano-sheets, leading to a large surface area and confined thickness at atomic scale [25,26]. Moreover, these nano-sheets not only produce huge catalytic active sites, but also cause quantum confinement effect on the movement of electron-hole pairs [20–22].

However, there were few reports on H_2 evolution using TiO_2 (B) nano-sheets as photocatalysts for hydrogen production. Kumar successfully achieved TiO_2 (B)-anatase mixed-phase titania nanorods by an effective annealing method. While the mixed-phase nanorods show high photocatalytic activity for H_2 production using Cu_2O as the co-catalyst, they exhibit little photocatalytic activity as P25 without the help of Cu_2O co-catalyst [27]. The band gap of the TiO_2 (B) nanorods was found to be about 3.2 eV, keeping almost the same as the one in the bulk material [27]. Given the enlarged band gap of 3.6 eV in TiO_2 (B) nanosheets [25], it is important to explore the H_2 production based on TiO_2 (B) nano-sheets and its composites.

In this work, we performed a systematic investigation on the growth of TiO_2 (B) nano-sheets and their effects on the hydrogen production by using the hydrothermal method. It was found that the ethanol/EG ratio in the solvent plays an important role in the crystal growth. At proper conditions, a new morphology of anatase quantum dots grown on the surface of TiO_2 (B) nano-sheets was successfully synthesized for the first time. Even without loading any co-catalysts, the TiO_2 (B)-anatase composite was shown to possess a high photocatalytic activity, about 45 times higher than that of commercially purchased Degussa P25. A detailed analysis on the microstructure, chemical bonding, and electronic structure reveals that the high photocatalytic activity is synergistically contributed by large specific surface area, abundant surface active sites, and properly aligned band structure. Especially, the accurate band alignment of TiO_2 (B)-anatase shows that the conduction band (CB) level of TiO_2 (B) is about 0.6 eV higher than that of anatase, providing a larger driving force for the reduction of water without the help of co-catalyst.

2. Experiments

2.1. Sample preparation

All purchased chemicals were analytical grade and used without further purification. The ultra-thin TiO_2 (B) nano-sheets, anatase TiO_2, and their composite were synthesized by the hydrothermal method. Solution A was prepared by adding 5 ml of titanium isopropoxide (TTIP) into 3 ml of HCl solution under stirring. Solution B was obtained by dissolving 1 ml of polyethylene oxid-polypropylene oxide-polyethylene oxide (Pluronic P123) in a certain amount of ethanol. After stirring for 15 min, solution B was added into solution A and stirred for another 30 min. Then, the mixed solution with a certain amount of EG was transferred into a 200 ml Teflon-lined autoclave and heated at 150 °C for 20 h. The volume ratios of ethanol to EG were 1/9, 5/5, 8/2, 10/0, and the corresponding samples were named as Et1, Et5, Et8, Et10, respectively. After hydrothermal reaction, the obtained products were centrifuged and washed with ethanol for three times, and then dried at 60 °C for 8 h.

2.2. Characterization

The powder X-ray diffraction (XRD) was carried out using a D8-Advance diffractometer with a Cu Kα radiation source ($\lambda = 0.15418$ nm). Raman spectroscopy was carried out on Renishaw In Via with an excitation laser of 532 nm to analyze the phase of the samples. The microstructure of the samples was characterized by field emission high-resolution transmission electron microscopy (FEI Tecnai G2 F30). The X-ray photoelectron spectra (XPS, ESCALAB 250Xi) of the samples were measured before water splitting experiments. The binding energies were corrected for surface charging by referencing to the designated hydrocarbon C 1s binding energy at 284.8 eV. Gaussian function was used for the least-squares curve fitting procedure. The ultraviolet photoelectron spectroscopy (UPS) was used to obtain the work function and the valence band maximum with respect to the Fermi level (E_F) of the samples, and the position of E_F was referenced to a gold standard [28]. UV–vis diffused reflectance spectra of the samples were obtained by the spectrophotometer (Japan SHIMADZU UV-3600) using $BaSO_4$ as reference. BET (Brunauer-Emmet-Teller) analysis was done on QDS-MP-30 Nitrogen adsorption apparatus to measure the specific surface areas.

2.3. Photocatalytic hydrogen production

Photocatalytic H_2 production experiments were carried out in a 200 ml Pyrex reaction flask at room temperature and ambient pressure. The openings of the flask were sealed with silicone rubber plugs. Catalyst sample of 20 mg was suspended in 80 ml of methanol aqueous solution, which is composed of 16 ml methanol and 64 ml H_2O in the reaction flask. A 350 W Xe arc lamp (XQ350, Shanghai Lancheng, China) with current of 15.0 A was used as light source to irradiate the flask. Prior to irradiation, the system was bubbled with nitrogen for 30 min to remove the air and dissolved oxygen. The reaction system was then irradiated by Xe arc lamp for several hours. A continuous magnetic stirrer was applied at the bottom of the reactor in order to keep the photocatalyst in suspending status during the whole period of experiment. Every 1 h, 1 ml of gas was sampled by the head space auto sampler through the silicone rubber plug, and the gas component was analyzed by gas chromatograph (GC-2018, Shimadzu, Japan, TCD) with column of 5 Å molecular sieve. Nitrogen was used as a carrier gas. Production of H_2 was calculated according to the retention time and peak area calibrated with standard H_2 gas.

3. Results and discussion

3.1. Phase component and specific surface area

The phases of the titania samples prepared under various ethanol and EG ratios have been determined by combining the XRD and Raman spectroscopy. Fig. 1 displays the XRD patterns of the as-prepared titania samples, together with the standard peaks of TiO_2 (B) (JCPDS 046-1237) and anatase (JCPDS 71-1168). Notice that the diffraction peaks of TiO_2 (B) at (110) and (020) are very close to those of anatase at (101) and (200), making it hard to distinguish them out. Fortunately, two peaks emerging at 15.2° and 28.6°, corresponding to the (200) and (002) planes of TiO_2 (B), can be used as monitors to indicate the existence of TiO_2 (B) (see Fig. S1). It is found that single anatase phase forms when ethanol is the only solvent, as shown in the XRD spectrum of Et10. As EG is introduced

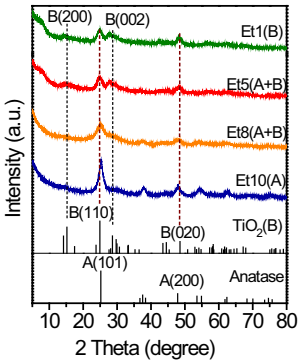

Fig. 1. XRD patterns of the samples Et1, Et5, Et8, and Et10. A and B in the brackets stand for the anatase and TiO_2 (B) phases, respectively.

into the solvent, TiO_2 (B) phase appears and the amount of TiO_2 (B) phase increases with increasing the fraction of EG. The peak of (200) plane in Et1 is broaden and its intensity is quite low, compared to the standard powder diffraction pattern of TiO_2 (B), indicating ultra thin thickness along the [200] direction. The corresponding crystal dimension along the a-axis could be determined from the FWHM at the (200) peak position according to Scherrer formula [29], and the calculated thickness is about 3.1 nm, implying that they are stacks consisting of about 3 monolayers on average. Although XRD could be used to determine the phase formation in the composite, however, it is hard to extract the mass ratio between TiO_2 (B) and anatase due to undistinguished peak positions.

Raman spectroscopy was used to further explore the phase information and mass ratio in these samples, due to its excellent sensitivity to the chemical compositions, phase transformation and crystallinity. The characteristic Raman peaks of TiO_2 (B) are located at 210, 256, 382, 422, 477, 553, 632, and 828 cm^{-1} [30], and those of anatase at 144, 197, 395, 516, and 638 cm^{-1} [31]. As shown in Fig. 2, all the Raman peaks of Et1 match well with the peaks of TiO_2 (B), indicating the formation of pure TiO_2 (B) phase, while Et10 displays only the characteristic Raman peaks of anatase, indicating the formation of pure anatase phase. These results are consistent with the XRD data presented in Fig. 1. Meanwhile, Et5 (the ratio of ethanol to EG is 5/5) and Et8 (the ratio of ethanol to EG is 8/2) exhibit the characteristic Raman peaks of both TiO_2 (B) and anatase, indicating the coexistence of both phases in the samples. The contributions of anatase and TiO_2(B) to the Raman intensities were extracted by fitting using Lorentzian peak profiles. The mass ratio of the mixed phases could be obtained by fitting the Raman peaks with equation [32]:

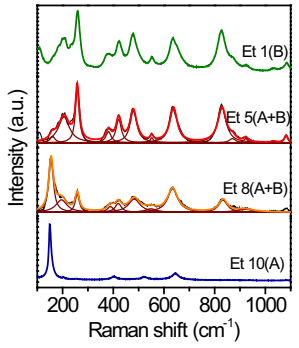

Fig. 2. Raman spectra of the samples Et1, Et5, Et8, and Et10. A and B in the brackets represent the anatase and TiO_2 (B) phases, respectively.

$$\frac{IA}{IB} = KR\frac{mA}{mB} \quad (1)$$

Where I_A and I_B are the Raman scattering intensities of the 144 cm^{-1} peak linked to anatase and the 256 cm^{-1} peak assigned to TiO_2 (B), and m_A and m_B are the relative mass of anatase and TiO_2 (B), respectively. The correlation factor of different phase contents K_R was calculated to be 6.57. The fitting results showed that Et5 (Et8) contains 1.7% (30.3%) anatase and 98.3% (69.7%) TiO_2 (B), respectively. The introduction of EG apparently suppressed the formation of anatase phase. When EG reached 80%, no anatase phase could be detected, and only pure TiO_2 (B) was formed.

Table 1 lists measurements of the phase ratio, specific surface area and pore volume for the samples. It is found that, the pore volume decreases as the anatase phase increases, indicating the increase of grain segregation. The specific surface area remains large in the range of 265–288 $m^2\ g^{-1}$ when anatase phase is less than 1.7%, and is reduced gradually when further increasing the anatase amount. The specific surface area for pure anatase is 167.63 $m^2\ g^{-1}$, about 3 times of 51 $m^2\ g^{-1}$, the specific surface area for the commercially purchased Degussa P25.

3.2. Photocatalytic hydrogen production from water splitting

Fig. 3a shows the rates of H_2 production from the water splitting reaction for the as-prepared samples and commercial Degussa P25, without adding any co-catalyst such as Pt. One can see that Et1 (single TiO_2 (B) phase) and Et10 (single anatase phase) exhibit relatively high mass specific activities of 690 and 98 $\mu mol \cdot h^{-1} \cdot g^{-1}$, respectively, about 23 and 3 times of that of P25 (30 $\mu mol \cdot h^{-1} \cdot g^{-1}$). For the TiO_2 (B)-anatase composite nanostructure, Et5 shows the largest mass specific activity of 1312 $\mu mol \cdot h^{-1} \cdot g^{-1}$, 45 times higher than that of P25. With increasing the reaction time up to 5 h, Et5 maintained a stable hydrogen production rate (see Fig. S2), demonstrating that the composite is robust photocatalyst without phase change or structure collapse during the irradiation process.

To explore the intrinsic mechanism for the enhancement of photoactivity, the surface specific activities of different samples are shown in Fig. 3b for comparison. One can clearly see that, except Et10 with a pure anatase phase and lower surface specific activity than that of P25, the other samples with a single TiO_2 (B) phase or TiO_2 (B)-anatase composite nanostructure have a larger surface specific activity than that of P25. In particular, Et5 still shows the largest surface specific activity of 4.55 $\mu mol \cdot h^{-1} \cdot m^{-2}$. These results indicate that, in addition to specific area, other factors, such as the density of active sites and interface between different phases, also play important roles in the photocatalytic reactivity.

3.3. Functionalities of microstructures and chemical bonds

The morphologies and microstructures of Et1 and Et5 measured by high resolution electron transmission microscopy are displayed in Fig. 4. In consistent with previous report [26], Et1 with the pure TiO_2 (B) phase shows a morphology of 2D corrugated ultrathin nano-sheets, as illustrated in Fig. 4a and b. The exposed surface crystal plane of Et1 could be read out from the HRTEM image shown in Fig. 4c: Lattice fringes of 2.08 Å and 1.87 Å are found to be perpendicular each other in a large area of the specimen, matching well with the d-spacings of (003) and (020) planes for TiO_2 (B), suggesting that the exposed surface of layered TiO_2 (B) nano-sheets is (100). The reported lattice parameters of a = 12.204 Å, b = 3.748 Å, c = 6.535 Å, $\alpha = \gamma = 90$, and $\beta = 107.36$ also indicate that the cleavage plane of TiO_2 (B) should be (100) in the b-c plane. The exposed (100) facet of nano-sheets is different from previous

Table 1
Phase composition, specific surface area S_{BET}, and pore volume of the as-prepared TiO_2.

Samples	Phase composition	$S_{BET}(m^2g^{-1})$	Pore volume (cm^3g^{-1})
Et1	Pure TiO_2 (B)	265.19	0.219
Et5	98.3% TiO_2 (B) and 1.7% anatase	288.21	0.190
Et8	69.7% TiO_2 (B) and 30.3% anatase	237.83	0.134
Et10	Pure anatase	167.63	0.122

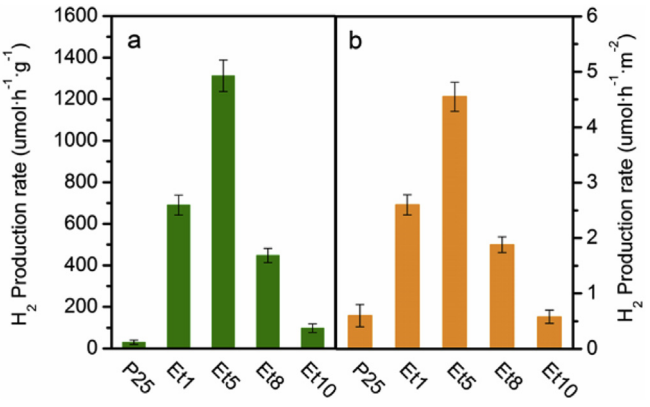

Fig. 3. Comparison of the H_2 production rates of samples P25, Et1, Et5, Et8 and Et10, (a) mass specific activity and (b) surface specific activity.

report, where the (010) facet of TiO_2 (B) nano-sheets was obtained by using $TiCl_3$ as the precursor [25]. In addition, bond breaking or bond distortion could be observed in the surface according to the HRTEM picture in Fig. 4c, which commonly appears in the corrugated ultrathin films [33,34]. This result is consistent with the XRD measurements, which indicate that the average thickness is about 3.1 nm. The thicknesses of the nano-sheets are further characterized by AFM measurements, as shown in Fig. S3. The obtained thicknesses are in the range from 1.1 nm to 3.3 nm corresponding to 1–3 monolayers, evidencing the formation of ultra thin films.

Fig. 4d–f presents the TEM pictures of Et5 with mixed phases. As seen in Fig. 4e, in addition to the basic nano-sheet structure, there are some nanoparticles aggregated on the surface with the individual particle sizes being about 3–5 nm in diameter. Fig. 4f displays the typical HRTEM image of one of aggregated nanoparticles. The lattice fringes are spaced by 1.89 Å and 2.39 Å and perpendicular to each other, corresponding to the (200) and (004) planes of anatase TiO_2. This indicates that the quantum dots of anatase TiO_2 self-assembly grow on the TiO_2 (B) (100) surface, with the exposed crystal plane of {010}. The atomic arrangement of TiO_2 (B) (100) and anatase (010) planes, as well as the atomic matching between the two planes, is schematically shown in Fig. 5. It is demonstrated that the lattice misfit is only 1% along the b-axis and 3.5% along the c-axis of TiO_2 (B), explaining the self-assemble growth mechanism. The crystal plane {010} of anatase TiO_2 was reported to exhibit the highest photocatalytic activity among all the facets of anatase due to the cooperative effect of surface atomic structure and surface electronic structure [35,36]. Hence, The exposed crystal plane of {010} of anatase in our work is expected to make a positive contribution to photocatalytic activity.

The chemical states and electronic band structures were studied

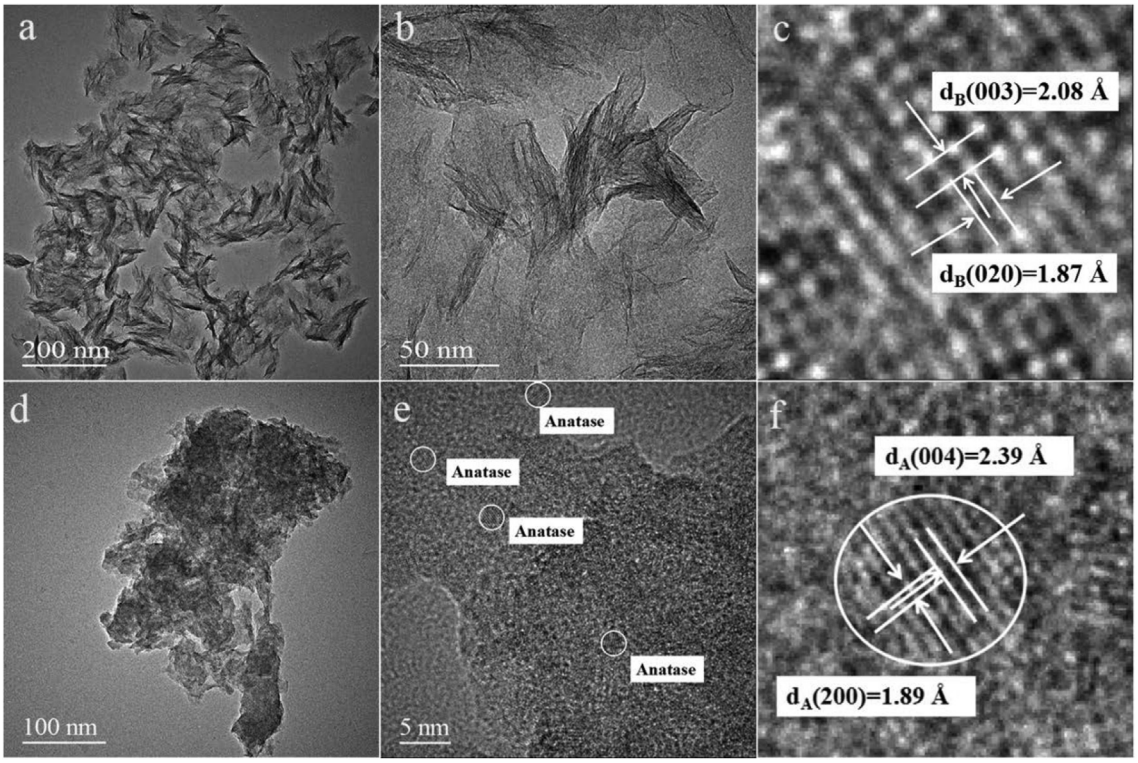

Fig. 4. (a,b) TEM images and (c) HRTEM image of ultrathin TiO_2 (B) nano-sheets in sample Et1; (d,e) TEM images and (f) HRTEM image of TiO_2 (B)-anatase composite in sample Et5.

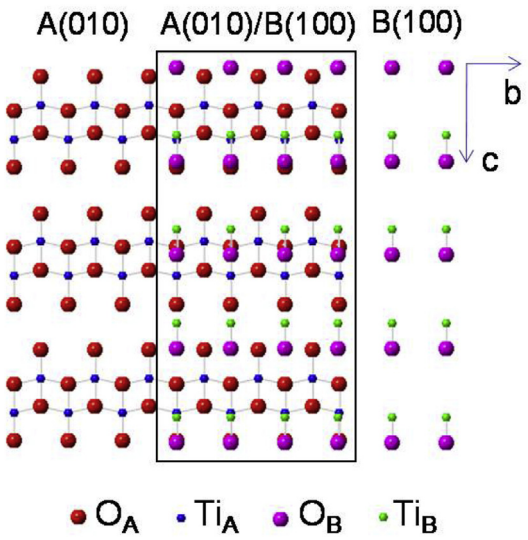

Fig. 5. The atomic arrangement and lattice matching between TiO_2 (B) (100) plane and anatase TiO_2 (010) plane. The two planes are labeled by B(100) and A(010), respectively.

to clarify the cause for the high photocatalytic activity. The Ti *2p* and the O *1s* XPS spectra of the typical samples are shown in Fig. 6a and b. All binding energies (BE) are referenced to the C *1s* peak at 284.6 eV. The binding energies of Ti *2p3/2* and Ti *2p1/2* in XPS spectra of Et1, Et5 and Et10 are given in Table 2. The core levels of Et10 are consistent with those of the referenced stoichiometric bulk anatase TiO_2 [37], indicating that they are related to Ti^{4+}. In contrast, the core levels of Et1 and Et5 are found to red shift to lower binding energies with the shift values of 0.7 eV and 1.0 eV, respectively, which is similar to the observed red shift of the binding energy in the ultrathin 2D nano-sheets [22]. The decrease of the binding energy signals the formation of Ti^{3+} state, which can enhance the reducibility to release electrons [38]. In the ultra-thin TiO_2 (B) nano-sheets, the high density defect states formed by bond insertion, bond breaking or bond distortion between metal and oxygen atoms are responsible for the Ti^{3+} formation [26,38].

The XPS spectra of O *1s* were de-convoluted into three constituents corresponding to different oxygen-containing chemical bonds: water molecule (H-*O*-H) at 532.5–533.1 eV, hydroxide (Ti-*O*-H) at 530.5–531.5 eV and oxide (Ti-*O*-Ti) at 529.3–530.0 eV [39–41]. Among them, the bridging hydroxyls (Ti-*O*-H) are known to come from the dissociative adsorption of water on oxygen vacancies, and the Ti ions connected to the -OH group is in the +3

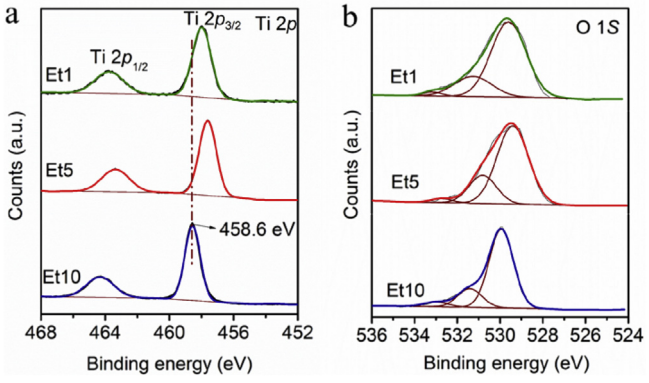

Fig. 6. The XPS spectra of the samples Et1, Et5, and Et10, (a) Ti *2p*; (b) O *1s*.

Table 2
Binding energies of Ti *2p3/2* and Ti *2p1/2* in XPS spectra for the samples Et1, Et5 and Et10.

Samples	Et1	Et5	Et10	Ref [32]
Ti *2p3/2* (eV)	457.9	457.6	458.6	458.6
Ti *2p1/2* (eV)	463.7	463.3	464.3	464.3
ΔE (eV)	5.8	5.7	5.7	5.7

valence state. Ti^{3+} acts as a Bronsted acid site to anchor water molecule to form strongly bounded OH-H_2O complex [41,42]. As a result, Ti^{3+} is then oxidized to Ti^{4+} by –OH filled in the vacancies. When exposed to light, photo-generated reducing electron can be easily transferred to water molecule at the active Ti-OH site to cause proton reduction. The percentage of the hydroxide chemical bond of Et5, Et1, and Et10 are estimated about 23.2%, 21.8%, and 18.2%, respectively. This partially explains the highest photocatalytic activity in Et5 and relatively low photocatalytic activity in Et10.

Based on the above analyses, high mass specific activities in Et1, Et5, and Et8 are intimately related to three factors: the nano-sheet structure, Ti^{3+} active sites, and Ti-OH sites on the surface of TiO_2 (B) phase. The first factor enlarges the specific surface area and offers a reduced distance for the photo-generated carriers to transport to the surface, leading to a decrease of carrier recombination probability. The later two factors promote the carrier separation and proton reduction. However, one critical question arising is why Et5 has a much higher photocatalytic activity than Et1, even though the two samples have close TiO_2 (B) (100) surface areas (see Table 1). To address this issue, we make an analysis of the effect of anatase quantum dots on the photocatalytic activity in the following section.

3.4. Effect of band structure on the water splitting

The band structures of TiO_2 (B) and anatase TiO_2 can be determined from the optical absorption and UPS spectra. Fig. 7a shows the optical absorption spectra obtained from the UV–vis diffused reflectance measurement for Et1-Et10 and P25. The band-gap values calculated from the corresponding modified Kubelka–Munk functions are shown in Fig. 7b [43]. The band gap takes the largest value of 3.5 eV for Et1 with a pure TiO_2 (B) phase, and is gradually reduced with decreasing the EG ratio, then reaches 3.22 eV for Et10 with a pure anatase phase, when no EG was added in the solvent. The obtained band gap value of the pure TiO_2 (B) nanosheets is 0.3 eV larger than the reported value of 3.2 eV in TiO_2 (B) nanorods [27], indicating a quantum confinement effect due to the ultra thin thickness of the TiO_2 (B) nanosheet.

Fig. 8a shows the UPS spectra of Et1 and Et10. The work functions for TiO_2 (B) in Et1 and anatase TiO_2 in Et10 are found to be 4.59 eV and 4.52 eV, and the valence band edges are 7.10 eV and 7.40 eV with respect to the vacuum energy level E_{vac}, respectively. In terms of these band parameters, the band alignments of single phase TiO_2 (B) and anatase TiO_2 are plotted in Fig. 8b. One can readily see that the bottom levels of conduction band of TiO_2 (B) and anatase TiO_2 are about 0.9 eV and 0.32 eV higher than that of the redox potential level of H^+/H_2 (0 V vs. NHE). The higher conduction band results in a larger driving force for reduction of water to form H_2, which makes a significant contribution to the higher photocatalytic activity in Et1 than in Et10.

When TiO_2 (B) contacts anatase TiO_2 to form a heterojunction as in Et5, their Femi levels align to the same position, and the corresponding heterojunction band structure can been drawn in Fig. 8c. The alignment of the Fermi level makes the difference of conduction band edges increases from 0.58 eV to 0.65 eV, leading to a

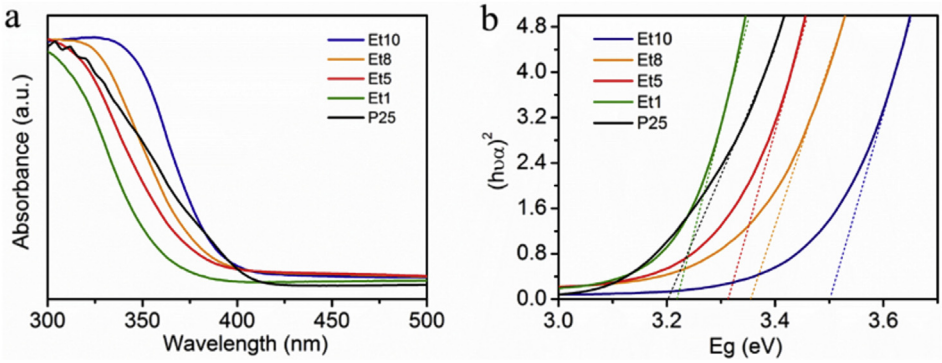

Fig. 7. (a) Diffuse reflectance UV–visible spectra and (b) corresponding Kubelka–Munk function plots for the samples Et1-Et10 and P25.

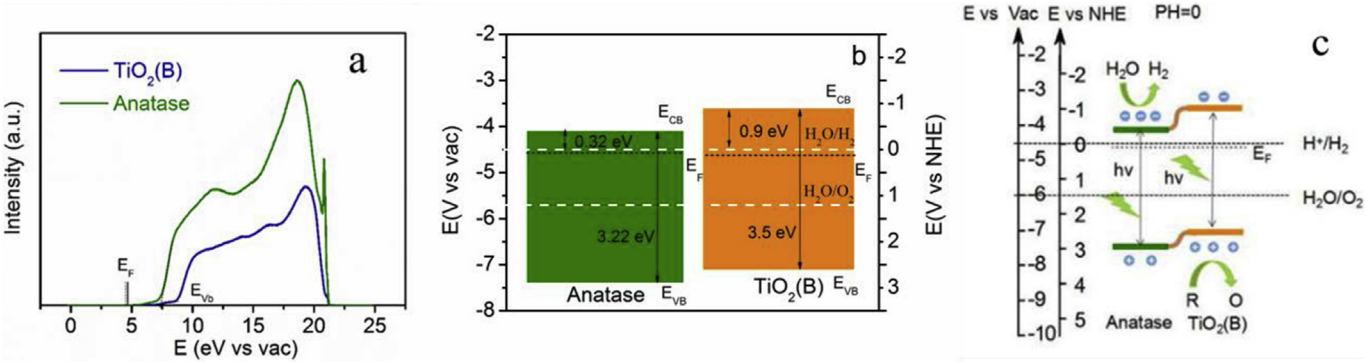

Fig. 8. (a) UPS spectra of TiO_2 (B) and anatase TiO_2. The energy is referenced to the vacuum level. (b) The band structures of single phase TiO_2 (B) and anatase TiO_2. (c) The band structure of TiO_2 (B)/anatase heterojunction.

higher driving energy for the transferred charge from TiO_2 (B) to anatase TiO_2. Moreover, it is found that there exist no potential well and potential barrier at the heterojunction interface, which provides a perfect carrier separation route and greatly reduces the carrier combination at the interface. Consequently, the photocatalytic activity in Et5 is dramatically enhanced by the combination of functionalities of the interface and active {010} surface of anatase TiO_2.

Compared to Et5, Et8 consisted of 69.7% TiO_2 (B) and 30.3% anatase has a much lower photocatalytic activity, which seems to contradict to the above analyses. The highly possible reason is that the increase of anatase proportion does not enlarge the interface between anatase and TiO_2 (B), and then the photocatalytic activity is strongly weakened by the decrease of TiO_2 (B) proportion. A similar phenomenon has been observed in the rutile/anatase composite [44]. In addition, obvious segregation of nanoparticles in Et8, as observed by TEM, also plays a negative role in the photocatalytic activity via the reduction of specific surface area.

4. Conclusion

In this work, ultra-thin corrugated TiO_2 (B) nano-sheets with the (100) exposed plane, were synthesized by the hydrothermal method. By adjusting the volume ratio between EG and ethanol in the solvent, a novel composite nanostructure with anatase quantum dots grown on the TiO_2 (B) nano-sheets was obtained. The measurement of hydrogen production showed that the TiO_2 (B) nano-sheets have a high phtocatalytic activity even without the help of co-catalyst, which is further enhanced by the composite nanostructure. A detailed analysis showed that the high phtocatalytic activity can be attributed to several advantages of TiO_2 (B) nano-sheets, including confined thickness in atomic scale, large specific surface area, abundant surface Ti^{3+} active sites, and a relatively high conduction band edge with respect to the redox potential level of H^+/H_2. In addition, the TiO_2 (B)-anatase composite nanostructure shows a type-II heterojunction band structure without potential well or barrier at the interface, which promotes the charge separation at the interface, leading to a further enhancement of phtocatalytic activity.

Notes

The authors declare no competing financial interest.

Acknowledgment

The authors are grateful to the National Science Foundation of China and the Ministry of Education, China for the financial support (Nos: 11374091, 11574076, 11274100, 11674087, 51602094), (20134208110005).

Appendix A. Supplementary data

Supplementary data related to this article can be found at http://dx.doi.org/10.1016/j.jpowsour.2017.06.021.

References

[1] A. Esswein, D. Nocera, Hydrogen production by molecular photocatalysis, Chem. Rev. 107 (2007) 4022–4047.
[2] A. Fujishima, Electrochemical photolysis of water at a semiconductor electrode, Nature 238 (1972) 37–38.
[3] F.E. Osterloh, Inorganic nanostructures for photoelectrochemical and

photocatalytic water splitting, Chem. Soc. Rev. 42 (2013) 2294–2320.
[4] Y. Ma, X. Wang, Y. Jia, X. Chen, H. Han, C. Li, Titanium dioxide-based nanomaterials for photocatalytic fuel generations, Chem. Rev. 114 (2014) 9987–10043.
[5] H. Xu, S. Ouyang, L. Liu, P. Reunchan, N. Umezawa, J. Ye, Recent advances in TiO_2-based photocatalysis, J. Mat. Chem. A 2 (2014) 12642–12661.
[6] Z. Zhao, J. Tian, Y. Sang, A. Cabot, H. Liu, Structure, synthesis, and applications of TiO_2 nanobelts, Adv. Mat. 27 (2015) 2557–2582.
[7] A. Kudo, Y. Miseki, Heterogeneous photocatalyst materials for water splitting, Chem. Soc. Rev. 38 (2009) 253–278.
[8] Y. Sang, Z. Zhao, J. Tian, P. Hao, H. Jiang, H. Liu, J.P. Claverie, Enhanced photocatalytic property of reduced graphene oxide/TiO_2 nanobelt surface heterostructures constructed by an in situ photochemical reduction method, Small 10 (2014) 3775–3782.
[9] X. Zhang, Y. Wang, B. Liu, Y. Sang, H. Liu, Heterostructures construction on TiO_2 nanobelts: a powerful tool for building high-performance photocatalysts, Appl. Catal. B Environ. 202 (2017) 620–641.
[10] Y. Wang, H. Sun, S. Tan, H. Feng, Z. Cheng, J. Zhao, A. Zhao, B. Wang, Y. Luo, J. Yang, J.G. Hou, Role of point defects on the reactivity of reconstructed anatase titanium dioxide (001) surface, Nat. Commun. 4 (2012) 375–381.
[11] J. Yang, D. Wang, H. Han, C. Li, Roles of Co-catalysts in photocatalysis and photoelectrocatalysis, Acc. Chem. Res. 46 (2013) 1900–1909.
[12] J. Zhang, Q. Xu, Z. Feng, M. Li, C. Li, Importance of the relationship between surface phases and photocatalytic activity of TiO_2, Angew. Chem. Int. Ed. 47 (2008) 1766–1769.
[13] G. Li, S. Ciston, Z.V. Saponjic, L. Chen, N.M. Dimitrijevic, T. Rajh, K.A. Gray, Synthesizing mixed-phase TiO_2 nanocomposites using a hydrothermal method for photo-oxidation and photoreduction applications, J. Catal. 253 (2008) 105–110.
[14] T. Ohno, K. Tokieda, S. Higashida, M. Matsumura, Synergism between rutile and anatase TiO_2 particles in photocatalytic oxidation of naphthalene, Appl. Catal. A Gen. 244 (2003) 383–391.
[15] D.O. Scanlon, C.W. Dunnill, J. Buckeridge, S.A. Shevlin, A.J. Logsdail, S.M. Woodley, C.R.A. Catlow, M.J. Powell, R.G. Palgrave, I.P. Parkin, G.W. Watson, T.W. Keal, P. Sherwood, A. Walsh, A.A. Sokol, Band alignment of rutile and anatase TiO_2, Nat. Mat. 12 (2013) 798–801.
[16] D.C. Hurum, A.G. Agrios, S.E. Crist, K.A. Gray, T. Rajh, M.C. Thurnauer, Probing reaction mechanisms in mixed phase TiO_2 by EPR, J. Electron. Spectrosc. Relat. Phenom. 150 (2006) 155–163.
[17] D.C. Hurum, A.G. Agrios, K.A. Gray, T. Rajh, M.C. Thurnauer, Explaining the enhanced photocatalytic activity of Degussa P25 mixed-phase TiO_2 using EPR, J. Phys. Chem. B 107 (2003) 4545–4549.
[18] H. Wang, L. Zhang, Z. Chen, J. Hu, S. Li, Z. Wang, J. Liu, X. Wang, Semiconductor heterojunction photocatalysts: design, construction, and photocatalytic performances, Chem. Soc. Rev. 43 (2014) 5234–5244.
[19] K. Maeda, K. Teramura, D. Lu, N. Saito, Y. Inoue, K. Domen, Noble-Metal/Cr_2O_3 core/shell nanoparticles as a cocatalyst for photocatalytic overall water splitting, Angew. Chem. 118 (2006) 7970–7973.
[20] F. Wang, Y. Wang, Y.-H. Liu, P.J. Morrison, R.A. Loomis, W.E. Buhro, Two-dimensional semiconductor nanocrystals: properties, templated formation, and magic-size nanocluster intermediates, Acc. Chem. Res. 48 (2015) 13–21.
[21] M. Xu, T. Liang, M. Shi, H. Chen, Graphene-like two-dimensional materials, Chem. Rev. 113 (2013) 3766–3798.
[22] M. Zhou, X.W. Lou, Y. Xie, Two-dimensional nanosheets for photoelectrochemical water splitting: possibilities and opportunities, Nano Today 8 (2013) 598–618.
[23] T.P. Feist, P.K. Davies, The soft chemical synthesis of TiO_2 (B) from layered titanates, J. Solid State Chem. 101 (1992) 275–295.
[24] W. Zhou, L. Gai, P. Hu, J. Cui, X. Liu, D. Wang, G. Li, H. Jiang, D. Liu, H. Liu, Phase transformation of TiO_2 nanobelts and TiO_2(B)/anatase interface heterostructure nanobelts, Crystengcomm 13 (2011) 6643–6649.
[25] Z. Sun, T. Liao, Y. Dou, S.M. Hwang, M.-S. Park, L. Jiang, J.H. Kim, S.X. Dou, Generalized self-assembly of scalable two-dimensional transition metal oxide nanosheets, Nat. Commun. 5 (2014) 3813–3821.
[26] G. Xiang, T. Li, J. Zhuang, X. Wang, Large-scale synthesis of metastable TiO_2 (B) nanosheets with atomic thickness and their photocatalytic properties, Chem. Commun. 46 (2010) 6801–6803.
[27] D.P. Kumar, N.L. Reddy, M.M. Kumari, et al., Cu_2O-sensitized TiO_2, nanorods with nanocavities for highly efficient photocatalytic hydrogen production under solar irradiation, Sol. Ener. Mat. & Sol. Cells 136 (2015) 157–166.
[28] O. Goscinski, Principles of ultraviolet photoelectron spectroscopy, in: J.W. Rabalais (Ed.), Wiley-Interscience Monographs in Chemical Physics, 1977. New York. Int. J. Quantum Chem. 13 (1978) 263–263.
[29] Q. Li, B. Guo, J. Yu, J. Ran, B. Zhang, H. Yan, J.R. Gong, Highly efficient visible-light-driven photocatalytic hydrogen production of cds-cluster-decorated graphene nanosheets, J. Am. Ceram. Soc. 133 (2011) 10878–10884.
[30] V. Etacheri, Y. Kuo, A. Van der Ven, B.M. Bartlett, Mesoporous TiO_2–B microflowers composed of (110) facet-exposed nanosheets for fast reversible lithium-ion storage, J. Mat. Chem. A 1 (2013) 12028–12032.
[31] T. Ohsaka, F. Izumi, Y. Fujiki, Raman spectrum of anatase TiO_2, J. Raman Spectrosc. 7 (1978) 321–324.
[32] T. Beuvier, M. Richard-Plouet, L. Brohan, Accurate methods for quantifying the relative ratio of anatase and TiO_2(B) nanoparticles, J. Phys. Chem. C 113 (2009) 13703–13706.
[33] M. Ibn-Elhaj, M. Schadt, Optical polymer thin films with isotropic and anisotropic nano-corrugated surface topologies, Nature 410 (2001) 796–799.
[34] P.C. Su, C.C. Chao, J.H. Shim, R. Fasching, F.B. Prinz, Solid oxide fuel cell with corrugated thin film electrolyte, Nano Lett. 8 (2008) 2289–2292.
[35] C. Chen, L. Xu, G.A. Sewvandi, T. Kusunose, Y. Tanaka, S. Nakanishi, Q. Feng, Microwave-assisted topochemical conversion of layered titanate nanosheets to {010}-faceted anatase nanocrystals for high performance photocatalysts and dye-sensitized solar cells, Cryst. Growth Des. 14 (2014) 5801–5811.
[36] J. Zhao, X.X. Zou, J. Su, P.P. Wang, L.J. Zhou, G.D. Li, Synthesis and photocatalytic activity of porous anatase TiO_2 microspheres composed of {010}-faceted nanobelts, Dalt. Trans. 42 (2013) 4365–4368.
[37] C. Liu, S. Yang, Synthesis of angstrom-scale anatase titania atomic wires, ACS Nano 3 (2009) 1025–1031.
[38] S. Wendt, P.T. Sprunger, E. Lira, G.K.H. Madsen, Z. Li, J. Hansen, J. Matthiesen, A. Blekinge-Rasmussen, E. Lægsgaard, B. Hammer, F. Besenbacher, The role of interstitial sites in the Ti 3d defect state in the band gap of titania, Science 320 (2008) 1755–1759.
[39] B. Erdem, R.A. Hunsicker, G.W. Simmons, E.D. Sudol, V.L. Dimonie, M.S. El-Aasser, XPS and FTIR surface characterization of TiO_2 particles used in polymer encapsulation, Langmuir 17 (2001) 2664–2669.
[40] G. Ketteler, S. Yamamoto, H. Bluhm, K. Andersson, D.E. Starr, D.F. Ogletree, H. Ogasawara, A. Nilsson, M. Salmeron, The nature of water nucleation sites on TiO_2 (110) surfaces revealed by ambient pressure x-ray photoelectron spectroscopy, J. Phys. Chem. C 111 (2007) 8278–8282.
[41] A. Naldoni, M. Allieta, S. Santangelo, M. Marelli, F. Fabbri, S. Cappelli, C.L. Bianchi, R. Psaro, V. Dal Santo, Effect of nature and location of defects on bandgap narrowing in black TiO_2 nanoparticles, J. Am. Chem. Soc. 134 (2012) 7600–7603.
[42] O. Bikondoa, C.L. Pang, R. Ithnin, C.A. Muryn, H. Onishi, G. Thornton, Direct visualization of defect-mediated dissociation of water on TiO_2 (110), Nat. Mat. 5 (2006) 189–192.
[43] L. Liao, Q. Zhang, Z. Su, Z. Zhao, Y. Wang, Y. Li, X. Lu, D. Wei, G. Feng, Q. Yu, X. Cai, J. Zhao, Z. Ren, H. Fang, F. Robles-Hernandez, S. Baldelli, J. Bao, Efficient solar water-splitting using a nanocrystalline CoO photocatalyst, Nat. Nano 9 (2014) 69–73.
[44] S. Bashir, A.K. Wahab, H. Idriss, Synergism and photocatalytic water splitting to hydrogen over M/ TiO_2 catalysts: effect of initial particle size of TiO_2, Catal. Today 240 (2015) 242–247.